Hermitian and non-Hermitian Weyl physics in synthetic three-dimensional piezoelectric phononic beams

Liangshu He,[1] Yan Li,[1] Bahram Djafari-Rouhani,[2] and Yabin Jin[1,*]

[1]*School of Aerospace Engineering and Applied Mechanics, Tongji University, 200092 Shanghai, China*

[2]*Institut d'Electronique, de Microélectonique et de Nanotechnologie, UMR CNRS 8520, Département de Physique, Université de Lille, 59650 Villeneuve d'Ascq, France*

(Received 2 December 2022; accepted 16 March 2023; published 11 April 2023)

Recently, the evolution of the Weyl point (WP) caused by the introduction of nonhermiticity into Weyl semimetals has aroused great research interest. We consider elastic flexural wave propagation in a phononic beam containing piezoelectric materials and introduce nonhermiticity through active regulation of external circuits. Considering a synthetic parameter space constituted by the one-dimensional Bloch wave vector and two geometrical parameters, we demonstrate that a double WP (DWP) arises at the band crossing. Then we study its evolution from the hermitic to nonhermitic situation under the effect of the active piezoelectric materials. We find that the DWP in the hermitic case evolves into a Weyl degenerate line and a Weyl hollow ring as concerns the real and imaginary parts of the Weyl frequencies, respectively. The formation mechanisms of the DWPs, lines, and rings are explained through the Hamiltonian of the system. Further, we observe the changes of the DWP and degenerate line in the transmission spectra of finite structures. Finally, we discuss the synthetic Fermi arc interface states through the analysis of the reflected phase vortices. In this paper, we provide insights into the high-dimensional Hermitian and non-Hermitian physics in elastic wave systems using synthetic dimensions.

DOI: 10.1103/PhysRevResearch.5.023020

I. INTRODUCTION

In condensed matter physics, Weyl semimetals are a peculiar class of three-dimensional (3D) quantum states [1–4] that exhibit linear dispersion relations in all spatial directions around specific points of the reciprocal space, called Weyl points (WPs) [5]. The integration of the Berry curvature around the WP gives access to a topological charge that can be associated with the Berry flux of a magnetic monopole. WPs with opposite topological charges usually appear in pairs and are connected by the Fermi arc which is the reciprocal space representation of the gapless unidirectional surface state at the Fermi energy [1,6]. Subsequently, the concept of Weyl semimetals was naturally extended to classical wave systems, including photonic [7,8], acoustic [9,10], and elastic [11] systems. Different from the linear band crossing that arises in simple WPs, the dispersion may be dominated by a quadratic term in the Hamiltonian at least in one momentum direction. In this case, the crossing belongs to the double WP (DWP) [12]. The DWP has been observed in chiral woodpile photonic crystals [13] and stoichiometric compound strontium silicide [14]. Furthermore, to overcome the difficulty in the calculation and experiments dealing with spatially 3D structures, the concept of synthetic dimensions was skillfully introduced to investigate high-dimensional physics based on low-dimensional spatial structures [11,15,16].

On the other hand, the non-Hermitian systems have become the focus of attention in recent years [17–21]. Indeed, the non-Hermitian Hamiltonian considering loss and possibly gain is a more realistic situation than the Hermitian Hamiltonian of a closed system. While loss may be naturally present in any structure, some active elements can be used to achieve gain in non-Hermitian systems. For elastic wave systems, an elegant way would rely on active regulation of lead-zirconate-titanate (PZT) external circuits (ECs) [22–25]. The realization of negative effective values including negative inductance, capacitance, resistance, or a combination of the three of them through a non-Foster electrical circuit has become a reliable way to develop space-time modulated metamaterials in recent years [26–28], and some experimental works have been successfully carried out [29–31]. One of the most important characteristics of non-Hermitian systems is the appearance of an exceptional point (EP), which is the transition point of a parity-time symmetric system from pure real eigenvalues to complex conjugate spectra [32,33], thus opening to phenomena such as asymmetric mode switching [34] and unidirectional invisibility [35], among others. Recently, it has been observed that the introduction of nonhermiticity in optical [36] and acoustic [37] systems will make the WP of the Hermitian case evolve into a Weyl exceptional ring, which is the continuous track of the EP in the reciprocal space. Although the general Hermitian and non-Hermitian Weyl physics have been widely discussed in optical and acoustic systems, research into elastic flexural wave systems is still lacking.

*083623jinyabin@tongji.edu.cn

Published by the American Physical Society under the terms of the Creative Commons Attribution 4.0 International license. Further distribution of this work must maintain attribution to the author(s) and the published article's title, journal citation, and DOI.

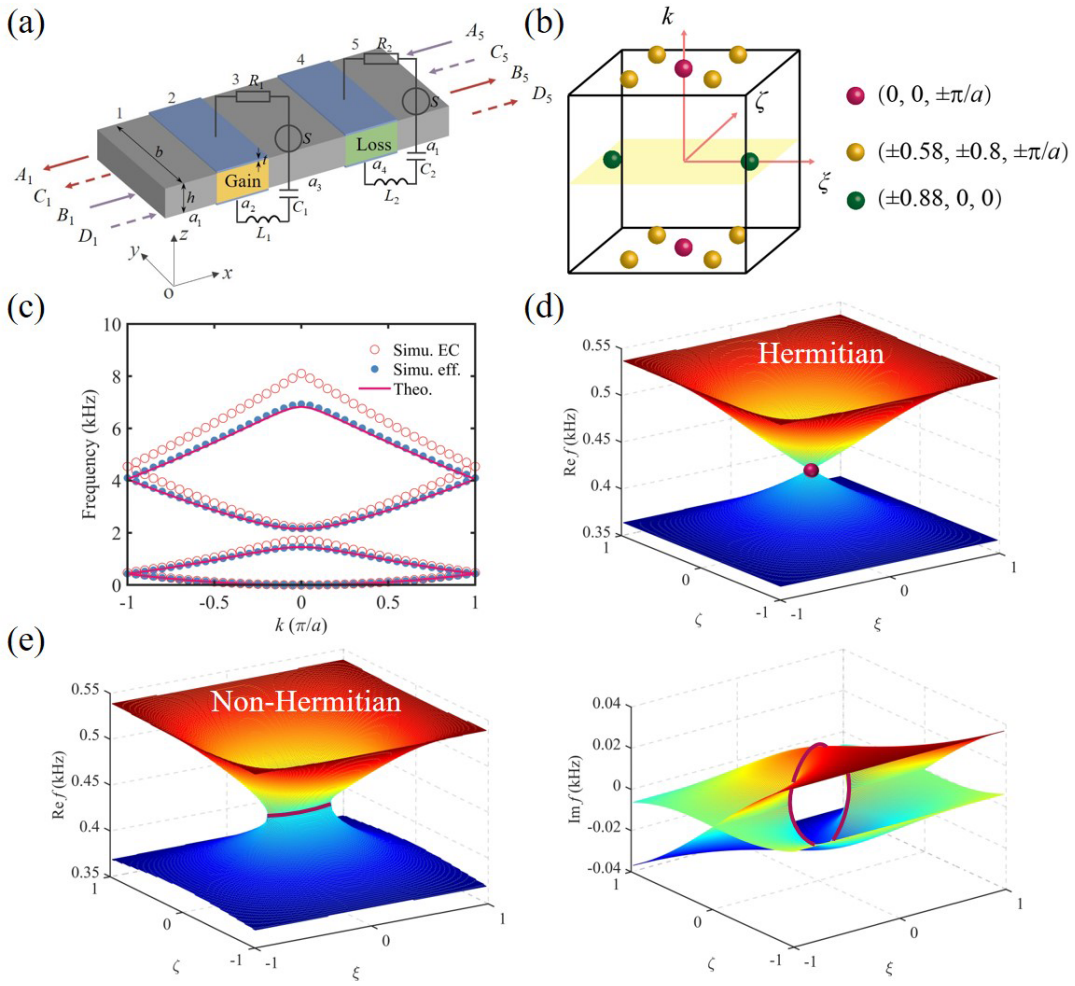

FIG. 1. (a) Schematic of the unit cell composed of three aluminum blocks and two lead-zirconate-titanate (PZT) blocks. The two PZT blocks colored in yellow and green are connected to external circuits (ECs) with copper electrodes. The arrows with solid and dashed lines represent the propagating and evanescent waves, respectively, and indicate the direction of wave propagation. The layers are numbered from 1 to 5. (b) Three-dimensional (3D) virtual parameter space composed of the wave vector k and synthetic parameters ξ and ζ. The three kinds of colored balls represent the double Weyl point (DWP) formed between different bands. (c) Simulated and theoretical band structures for $\xi = \zeta = 0$. The red circles, blue dots, and red solid lines, respectively, correspond to simulation with PZT EC, simulation using PZT effective modulus parameters, and theoretical calculation. (d) Band structure in the $\xi - \zeta$ space at $k = \pm\pi/a$ for the hermitic case. The red ball denotes DWP. (e) For the nonhermitic case, the left and right panels represent, respectively, the real and imaginary parts of the spectrum in the $\xi - \zeta$ space at $k = \pm\pi/a$. The real and imaginary parts, respectively, form a Weyl degenerate line (WDL) and a Weyl hollow ring (WHR). The colors of the surfaces in (d) and (e) indicate the frequency, with an increase from blue to red.

In this paper, we further extend the exploration of the Hermitian and non-Hermitian Weyl physics to elastic phononic systems [38,39] by introducing nonhermiticity through active regulation of piezoelectric materials in a phononic beam. We realize the Weyl physics in a synthetic 3D space constituted by the one-dimensional (1D) reciprocal space and two geometrical parameters. We found that the introduction of the non-Hermitian factor will lead to the evolution of the DWP into the Weyl degenerate line (WDL) and Weyl hollow ring (WHR), describing the evolution of the real and imaginary parts of the frequency, respectively. We propose a Hamiltonian that gives a physical explanation of the trends in the DWPs, lines, and rings. We further observe the changes of the DWP and WDL in the transmission spectra of a finite phononic beam. Finally, we discuss the reflected phase vortices around the DWP and WDL and demonstrate the synthetic Fermi arc interface states that are guaranteed by these vortices.

II. MODEL AND FORMULATION

Figure 1(a) gives a schematic view of the phononic beam where each unit cell is constituted by two piezoelectric blocks (PZT-5H) sandwiched between three aluminum blocks. The calculations are based on three levels of approaches. One is the full simulation of the elastic beam structure including the piezoelectricity of PZT blocks and the external electric circuits. In a second simulation approach, the properties of the piezoelectric blocks are approximated by effective parameters following the effective modulus theory of Farhat *et al.* [22], as explained in Appendix A. A third analytical approach presented below describes the flexural waves of the metabeam

based on the Timoshenko beam theory. Here, the material parameters of aluminum are Young's modulus $E = 70$ GPa, Poisson's ratio $\nu = 0.33$, and density $\rho = 2700\,\mathrm{kg/m^3}$. We set the effective parameters of PZT as $E_0^{\mathrm{eff}} = 55GPa$, $\rho = 7500\,\mathrm{kg/m^3}$, and after equivalence, the Poisson's ratio 0.1704 and shear modulus 23.5 GPa. The geometric parameters of the structure are the lattice constant $a = 90$ mm and the sides of the beam $b = h = 50$ mm. We further assume $2a_1 + a_3 = 2a/3$ and $a_2 + a_4 = a/3$ and define two new parameters as $\xi = \frac{2a_1 - a_3}{2a_1 + a_3}$ and $\zeta = \frac{a_2 - a_4}{a_2 + a_4}$ which will constitute our synthetic parameters. Since the layer lengths are necessarily positive, both ξ and ζ are in the range [-1, 1]. Additionally, the wave vector is defined in the 1D Brillouin zone (BZ) related to the period of the structure, and its range is $[-\pi/a, \pi/a]$. The two synthetic dimensions and one physical dimension can construct a virtual 3D parameter space, as shown in Fig. 1(b).

We start with the case $\xi = \zeta = 0$ and employ the transfer matrix method to obtain the band structure of the phononic beam, as shown by the red solid lines in Fig. 1(c). Details about the theoretical derivation of the Timoshenko theory and transfer matrix calculations are provided in Appendix B; we use finite element simulation to verify the accuracy of the theoretical calculation, including simulation using PZT effective modulus parameters (blue dots) and simulation with full PZT EC (red circles). For the former, the material parameters of the piezoelectric blocks are set as equivalent parameters during simulation, while for the latter, the following simulation modeling is adopted using the Comsol Multiphysics software: the upper and lower surfaces of the PZT blocks are coated with copper electrodes of thickness $t = 0.1$ mm connected to two circuits, respectively, as shown in Fig. 1(a). Each circuit contains an AC voltage source and variable resistor, inductor, and capacitor. Their specific values are derived from the chosen modulus parameters, as explained in Appendix A. It can be seen in Fig. 1(c) that the results of the three methods show good agreement, supporting the correctness of our theoretical derivation based on the Timoshenko beam theory. Therefore, we choose the Timoshenko theory to carry out our research in the rest of this paper. It is worth noting that the band crossing of Fig. 1(c) exhibits degenerate points at the boundaries of the BZ ($k = \pm\pi/a$) which arise from a band-folding effect. Indeed, with $\xi = \zeta = 0$, the original unit cell of Fig. 1(a) is composed of two identical half-unit cells. If we fix the wave vector to $k = -\pi/a$ or π/a and scan the two synthetic parameters, as shown in Fig. 1(d), a degenerate point with cone intersection will be formed by the first and second bands in the $\xi - \zeta$ space, which is the so-called DWP; its frequency is 430 Hz and corresponds to the red balls in Fig. 1(b). Similarly, the third and fourth bands will form DWPs at $(0,\ 0,\ \pm)$ and $(\pm 0.58,\ \pm 0.8,\ \pm\pi/a)$, corresponding to the red and yellow balls in Fig. 1(b), respectively. Additionally, if we fix $k = 0$, DWPs can be found at $(\pm 0.88,\ 0,\ 0)$ formed by second and third bands, corresponding to the green balls in Fig. 1(b). Additional results about DWPs are provided in Appendix C.

In the following, we shall focus on the DWP formed by the first two bands at $k = -\pi/a$ and π/a. By adjusting the resistance and reactance of the two ECs, respectively, we can make the effective moduli of the PZT blocks complex, and a non-Hermitian system with both gain and loss can be constructed. Here, we adjust the effective Young's modulus of gain and loss to $E_{\mathrm{gain}}^{\mathrm{eff}} = E_0^{\mathrm{eff}}(1 - \gamma i)$ and $E_{\mathrm{loss}}^{\mathrm{eff}} = E_0^{eff}(1 + \gamma i)$, respectively, where the nonhermiticity parameter γ is arbitrarily fixed to 0.3 without loss of generality. The resulting effective Poisson's ratios and shear moduli (see Appendix A) become $\upsilon_{\mathrm{gain}}^{\mathrm{eff}} = 0.1704 - 0.3511i$, $\upsilon_{\mathrm{loss}}^{\mathrm{eff}} = 0.1704 + 0.3511i$, $G_{\mathrm{gain}}^{\mathrm{eff}} = 23.5 - 3.7 \times 10^{-4}i$, and $G_{\mathrm{loss}}^{\mathrm{eff}} = 23.5 + 3.7 \times 10^{-4}i$ GPa. If we scan the $\xi - \zeta$ space, the DWP of the hermitic case evolves into a WDL at the frequency of 436 Hz [left panel of Fig. 1(e)]. In addition, the imaginary part of the frequency is no longer zero but forms a WHR [right panel of Fig. 1(e)]. More information about the WDL and WHR is provided in Appendix C.

To explain the DWP in the hermitic case and its evolution to line and ring phenomena in the nonhermitic case, we propose the following Hamiltonian of the system [40]:

$$H(\xi, \zeta, k) = \begin{bmatrix} \omega_0(1 + m\zeta) - i\Gamma_0 + i\Gamma & \kappa(\xi, k) \\ \kappa^*(\xi, k) & \omega_0(1 - m\zeta) - i\Gamma_0 - i\Gamma \end{bmatrix}, \tag{1}$$

where ω_0 is the original ($\zeta = 0$) first nonrigid-body resonance frequency of the PZT blocks, $i\gamma$ and $-i\Gamma(\Gamma = \tau\gamma \geqslant 0)$ denote the gain and loss modulation, respectively, τ is a coefficient connecting nonhermitic parameters γ and Γ, $-i\Gamma_0(\Gamma_0 \geqslant 0)$ denotes the intrinsic loss, and $\kappa(\xi, k) = \kappa_+(\xi) + \kappa_-(\xi)e^{-ika}$, with $\kappa_+(\xi) = \kappa_0(1 + n\xi)$ and $\kappa_-(\xi) = \kappa_0(1 - n\xi)$ representing the intracell and intercell coupling strengths; here, κ_0 is the original ($\xi = \zeta = 0$ and $\gamma = 0$) coupling strength, κ^* is the conjugate of κ, and m and n are two coefficients that control the resonance frequency shift and coupling strength, respectively. The eigenfrequencies of Eq. (1) take the following form:

$$\tilde{\omega}_{1,2} = \omega_0 - \Gamma_0 i \pm \sqrt{\kappa\kappa^* - (\tau\gamma - m\omega_0\zeta i)^2}, \tag{2}$$

where $\kappa\kappa^* = 4\kappa_0^2[(\cos\frac{ka}{2})^2 + n^2\xi^2(\sin\frac{ka}{2})^2]$. If we set $k = -\pi/a$ or π/a as before, this expression simplifies to $\kappa\kappa^* = 4\kappa_0^2 n^2\xi^2$. It is worth mentioning that the dispersion around these points are linear with respect to ζ and quadratic with respect to k and ξ. This can be easily demonstrated by calculating the first and second derivatives of $\tilde{\omega}_{1,2}$ with respect to the corresponding variables (see Appendix C). Since the DWP or the resulting WDL correspond to a degeneracy in the real part of the eigenfrequencies, the expression in the square root of Eq. (2) should be real and negative. This implies that (i) $m\omega_0\tau\gamma\zeta = 0$ and (ii) $4\kappa_0^2 n^2\xi^2 - \tau^2\gamma^2 + m^2\omega_0^2\zeta^2 \leqslant 0$. The first condition is satisfied if either $\gamma = 0$ (hermitic system) or $\zeta = 0$. In the hermitic case of $\gamma = 0$, the second condition will imply $\xi = \zeta = 0$, which reveals the formation

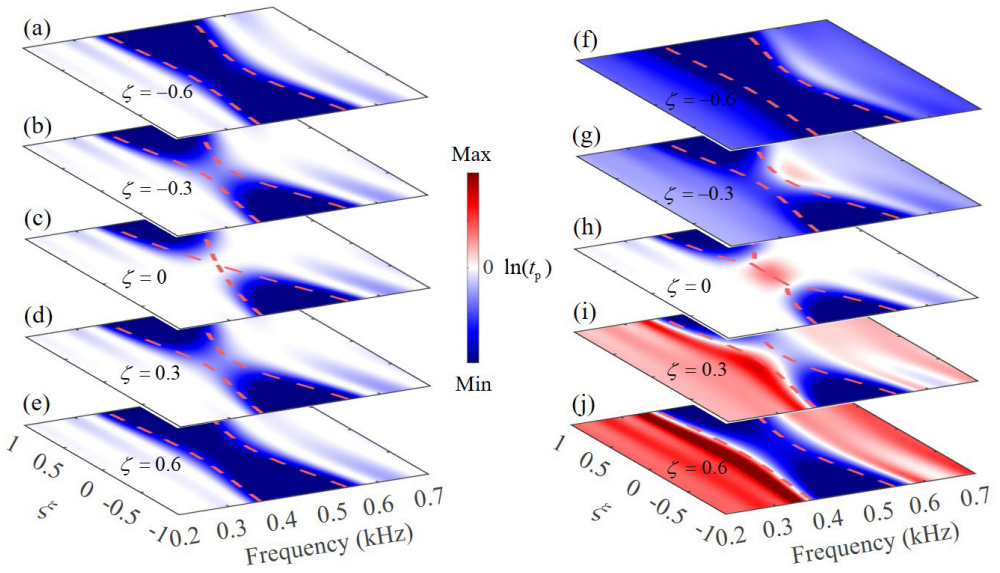

FIG. 2. Transmission spectra with different synthetic parameters ξ and ζ. The orange dashed lines are the band structures. (a)–(e) For the hermitic case and (f)–(j) for the nonhermitic case, showing the evolution processes of the double Weyl point (DWP) and Weyl degenerate line (WDL), respectively.

of DWP, as shown in Fig. 1(d). On the other hand, if $\zeta = 0$, condition (ii) yields $-\frac{\tau\gamma}{2\kappa_0 n} \leqslant \xi \leqslant \frac{\tau\gamma}{2\kappa_0 n}$, which reveals the formation of WDL in the real part of the frequency, as shown in the left panel of Fig. 1(e). So far, the eigenfrequencies can be simplified as $\tilde{\omega}_{1,2} = \omega_0 - \Gamma_0 i \pm \sqrt{\tau^2\gamma^2 - 4\kappa_0^2 n^2 \xi^2 i}$. We now set $f_i = \pm\sqrt{\tau^2\gamma^2 - 4\kappa_0^2 n^2 \xi^2} - \Gamma_0$, and further, through simple derivation, we can get

$$\frac{(f_i + \Gamma_0)^2}{(\tau\gamma)^2} + \frac{\xi^2}{\left(\frac{\tau\gamma}{2\kappa_0 n}\right)^2} = 1. \tag{3}$$

Equation (3) is an elliptic equation in the $f_i - \xi$ plane and reveals the formation of a WHR in the imaginary part of the frequency, as shown in the right panel of Fig. 1(e). It is worth noting that τ and n are fitting coefficients that can be adjusted according to actual parameters; therefore, this model can achieve accurate description of a DWP, WDL, and WHR.

III. OBSERVATION OF WEYL PHENOMENON IN FINITE STRUCTURES

A. DWP and WDL

We now consider a finite structure consisting of 9 units to observe and discuss the evolutions of the DWP and WDL in the transmission spectra. Details about transmission spectra calculation are provided in Appendix B. We calculate the transmission spectra of the propagating waves for different values of ζ. For the hermitic case [Figs. 2(a)–2(e)], the gradual increase of ζ from negative values results first in a decrease of the band gap that closes at $\zeta = 0$, before opening again and increasing for positive ζ. This behavior is consistent with the appearance of DWP from the band structure calculation shown by the orange dashed lines. Similarly, for the nonhermitic case, shown in Figs. 2(f)–2(j), the closing of the band gap coincides with a degenerate line instead of a point. Its length and frequency are consistent with the eigenfrequency result of Fig. 1(e). This can be seen from slices of Figs. 1(d) and 1(e) as illustrated in Appendix C. It is worth noting that the parameter ζ controls the amount of gain and loss in the system since it defines the relative lengths of the two PZT blocks. For the hermitic case where $\gamma = 0$, there is no gain or loss in the system, and the transmission in the passbands is always ~ 1 [$\ln(t_p) = 0$]. However, for the nonhermitic case, if $\zeta < 0$, then $a_2 < a_4$, so the overall gain of the system is less than the loss, and the transmission for passband is almost < 1. On the contrary, if $\zeta > 0$, then $a_2 > a_4$, so the overall gain exceeds the loss, and the transmission in the passbands is almost > 1. However, if $\zeta = 0$, the gain and loss are balanced, so the transmission for passband is ~ 1 [Fig. 2(h)].

B. Reflected phase vortices and synthetic Fermi arc interface states

In the following, we discuss the properties of the reflected phase around the DWP and WDL and their consequences for the Fermi arcs. For the hermitic case, the reflected phase [see Fig. 3(a)] exhibits a vortex distribution around the DWP at $\xi = \zeta = 0$ [15]. In this figure, we assume that the incident wave is at the DWP frequency (430 Hz) and calculate the reflected phase by scanning the ξ $-\zeta$ space. Similarly, in Figs. 3(b) and 3(c), we present the reflected phase distribution in the nonhermitic situation with a complex frequency incident wave at $(436 \pm 25i)$ Hz, where the real part is the middle frequency of the WDL and the positive (negative) imaginary parts correspond to the maximum (minimum) frequencies in the WHR [see Fig. 1(e)]. It can be seen that the reflected phase still exhibits a vortex distribution. The influence of nonhermiticity is essentially to shift the vortex centers toward $\xi < 0$ ($\xi > 0$) for positive (negative) imaginary parts of the incident wave frequency.

Another illustration of the winding behavior of the reflected phase is presented in Fig. 3(d), where we report φ as a

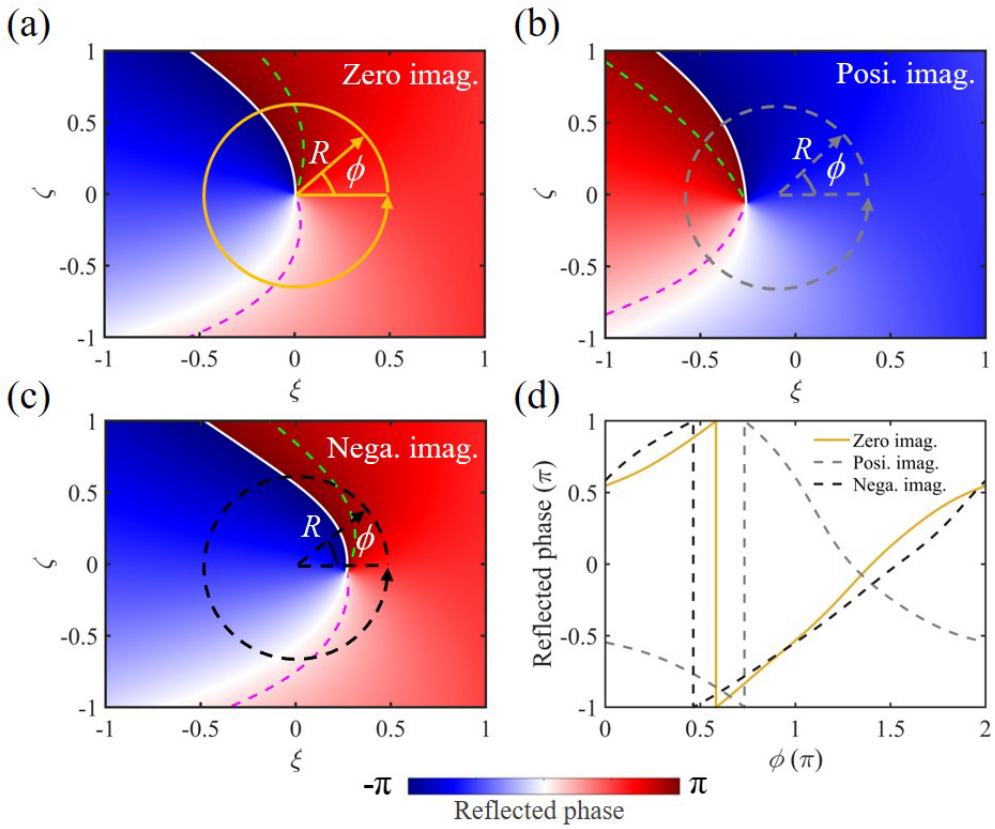

FIG. 3. Reflected phase vortex in synthetic $\xi-\zeta$ space. (a) Reflected phase vortex excited at the double Weyl point (DWP) frequency. (b) and (c) Reflected phase vortex excited at the middle frequency of the Weyl degenerate line (WDL); the results of the excitation of frequencies with (b) positive and (c) negative imaginary parts. The green and magenta dashed lines are the continuous change tracks of Fermi arc interface state formed when the reflected phase is 0.9π and 0.1π, respectively. The yellow, gray, and black circles have their centers at $\xi = \zeta = 0$ and a radius $R = 0.5$. (d) The changes of reflected phase as a function of the polar angle along the three circles in (a)–(c).

function of the polar angle ϕ around a circle of radius $R = 0.5$ in the $\xi-\zeta$ plane. Such circles are drawn in Figs. 3(a)–3(c), respectively, in yellow, gray, and black colors. Since the selected loops encircle the vortex centers, the reflected phase along these loops will cover a change of 2π, as summarized in Fig. 3(d). Let us note that the reflected phase vortex around the DWP has the same topological charge as the DWP [15]. The topological charge is defined as the integral of Berry curvature enclosing the DWP. However, it can be judged from an intuitive view that the topological charge corresponding to the clockwise and counterclockwise vortices for the DWP are, respectively, -2 and 2 [3,37,41]. The vortices created by two excitations with opposite signs of the imaginary parts of the frequency exhibit opposite windings.

According to the existence condition of an interface state between two media, established by the condition on the reflected phase, i.e., $\varphi_A + \varphi_B = 2m\pi\,(m \in Z)$ [42], one can find many combinations of parameters to create an interface between two different phononic beams supporting a localized state. Indeed, let us choose a reference phononic beam with a certain value of the reflected phase. Then the opposite of this phase can be found along a continuous trajectory starting from the vortex center. This trajectory will be the synthetic analog of the Fermi arc [15]. As a matter of illustration, we choose two such reference systems with reflected phases of $\varphi = -0.9\pi$ and $\varphi = -0.1\pi$ located on the circles of $R = 0.5$. Then we present in Figs. 3(a)–3(c) the trajectories that represent the opposite phases of 0.9π (0.1π) by the green (magenta) dashed lines. These trajectories start from the vortex center and end at the boundary of the space parameter. This is in contrast to the Fermi arcs in periodic structures that link two DWPs of opposite charges and results from the absence of periodicity in the synthetic parameter space. It is worth noting that DWPs with opposite charges can be found in the higher-frequency bands, which ensures the appearance of a complete Fermi arc. Some illustrations are provided in Appendix D.

Furthermore, we verify the Fermi arc interface states through theoretical calculations. We construct an interface between two beams where the left beam is one of the two reference systems mentioned above [with phase reflection of -0.9π $(-0.1\,\pi)$ on the circle of $R = 0.5$] and the right beam belongs to the Fermi arcs formed by the reflection phase of 0.9π $(0.1\,\pi)$ represented by the green (magenta) dashed lines in Fig. 3. The beams on the left and right sides of the interface contain 5 units, respectively. We calculate the interface state frequencies for a series of configurations on the Fermi arcs, as shown by the dots, stars, and circles in Fig. 4. For the hermitic case, the frequencies of the interface state are almost the same as the DWP frequency [see Fig. 4(a)]. For the nonhermitic

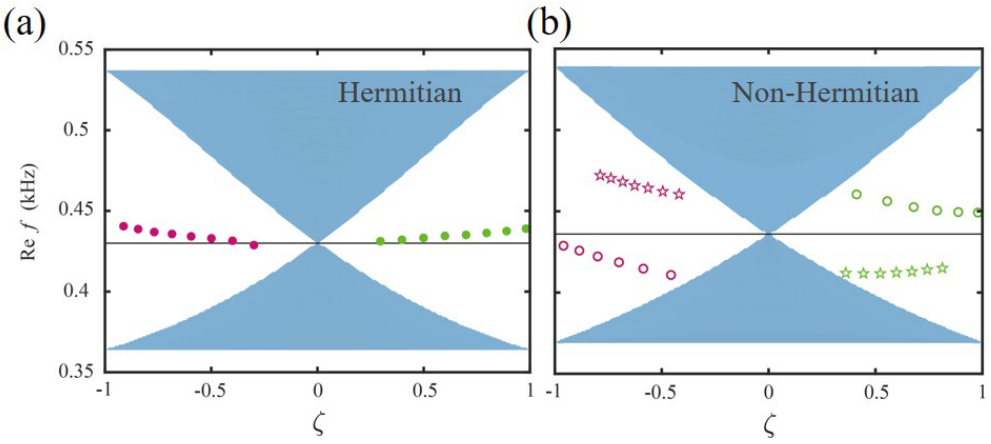

FIG. 4. Theoretical calculation for Fermi arc interface state frequencies for (a) the hermitic and (b) the nonhermitic case. The black horizontal lines in (a) and (b) are the double Weyl point (DWP) and the Weyl degenerate line (WDL) frequency, respectively. The dots in (a) correspond to the Fermi arcs in Fig. 3(a), while the stars and circles in (b) correspond to the Fermi arcs in Fig. 3(b) and 3(c), respectively. Green and magenta correspond to the Fermi arcs formed by $\varphi = 0.9\pi$ and $\varphi = 0.1\pi$, respectively.

case, the interface states display stronger shifts from the WDL frequency. The sign and magnitude of the shift depend on the sign of the imaginary part of the frequency and the relative magnitude of the gain and loss in the system. Specifically, for the interface state frequencies with a positive imaginary part, if the gain is greater than the loss ($\zeta > 0$), the interface state frequencies will shift down, and if the gain is less than the loss ($\zeta < 0$), the interface state frequencies will shift up [see the stars in Fig. 4(b)]. For the interface state frequencies with a negative imaginary part, the phenomenon is opposite [see the circles Fig. 4(b)].

IV. CONCLUSIONS

In conclusion, we discussed the existence of DWPs in a synthetic 3D space based on a 1D phononic beam and their transformations under the effect of nonhermiticity resulting from piezoelectric materials attached to ECs. We demonstrated theoretically the formation of a DWP, WDL, and WHR. Through the eigenderivation of the Hamiltonian, we proved the formation of the DWP in the Hermitian beam and the WDL and WHR in the non-Hermitian beam, respectively. We observed the change of the transmission spectrum of finite structures in the vicinity of the DWP and WDL and further discussed the reflected phase vortices around them. We found that the influence of nonhermiticity is the shift of vortex center without destroying the vortex structure. Both Hermitian and non-Hermitian reflected phase vortices cover 2π, ensuring the existence of synthetic Fermi arc interface states. In this paper, we extend the Hermitian and non-Hermitian Weyl physics to a synthetic elastic 3D system by using piezoelectric elements, which is a widely used platform in functional solid devices and provides insights for the high-dimensional non-Hermitian physics of elastic waves.

ACKNOWLEDGMENTS

This paper is supported by the National Natural Science Foundation of China (Grant No. 12272267), the Young Elite Scientists Sponsorship Program by CAST (Grant No. 2021QNRC001), and the Shanghai Science and Technology Committee (Grants No. 22JC1404100 and No. 21JC1405600), the program for the professor of special appointment (Eastern Scholar) at Shanghai Institutions of Higher Learning, the Fundamental Research Funds for the Central Universities.

APPENDIX A: EFFECTIVE MODULUS OF PZT BLOCK IN ECs

In this section, we describe how the equivalent method described in Ref. [22] can be applied to our problem to define the effective parameters of our piezoelectric materials and the resistance and reactance needed in the ECs. In Ref. [22], the equivalent modulus of piezoelectric materials is determined by the resistance and inductance of the EC. In this paper, we specify the equivalent modulus of the piezoelectric materials and use the relationship in Ref. [22] to derive the circuit parameters. Different from Ref. [22], to increase the adjustability of the circuit, we add capacitors in the circuit. The capacitance and inductance together provide the reactance of the circuit.

For a specific equivalent Young's modulus E^{eff}, the impedance in the EC should be [22]

$$Z = \frac{\left(s_{xx}^{E} - \frac{1}{E^{\text{eff}}}\right)h}{\left[d_{xz}^{2} - \varepsilon_{zz}^{T}\left(s_{xx}^{E} - \frac{1}{E^{\text{eff}}}\right)\right]\omega A_i i}, \tag{A1}$$

where $d_{xz} = -2.74 \times 10^{-10} C/N$ is a piezoelectric constant, $s_{xx}^{E} = 1.65 \times 10^{-11} Pa^{-1}$ is an element of the piezoelectricity compliance matrix, $\varepsilon_{zz}^{T} = 2000\varepsilon_0$ is the dielectric constant, $\varepsilon_0 = 8.854 \times 10^{-12} F/m$ is the permittivity of free space, $A_{2(4)} = ba_{2(4)}$ is the area of the PZT patch, $h = 50$ mm is the height of the metabeam, and ω denotes the angular frequency.

By using Eq. (A1), we can get the equivalent Poisson's ratio as $\nu^{\text{eff}} = -E^{\text{eff}} s'_{xy}$, where $s'_{xy} = s_{xy}^{E} - \frac{i\omega d_{xz}^{2} AZ}{h + i\omega \varepsilon_{zz}^{T} AZ}$ is an element of effective compliance matrix; here, $s_{xy}^{E} = -4.78 \times 10^{-12} Pa^{-1}$, and the equivalent shear modulus is $G^{\text{eff}} = \frac{E^{\text{eff}}}{2(1+\nu^{\text{eff}})}$. The impedance can be expressed as

$$Z = R + iX, \tag{A2}$$

where R is the resistance, $X = \omega L - \frac{1}{\omega C}$ is the reactance consisting of an inductive and a capacitive part. From Eq. (A1), we can determine the specific inductance, capacitance, and resistance which should be applied in the circuit to achieve the desired equivalent modulus. Let us note that, according to Eq. (A2), these quantities need to be adjusted when varying the frequency. Also, the same reactance can be realized for different combinations of L and C.

By setting the values of $E_{\text{gain}}^{\text{eff}}$ and $E_{\text{loss}}^{\text{eff}}$, the corresponding Poisson's ratios and shear moduli can be derived from the above equivalent theory as well as the required resistance and reactance values in both ECs. Since we need to achieve elastic wave gain, negative effective values are necessary to achieve in practical experiments. As we mentioned in the introduction, a non-Foster circuit can be a reliable solution to achieve negative equivalent electrical parameters. The interest and added value of non-Foster circuits is that the loss/gain can actively be tuned by negative/positive sign of resistance, and when an inductance and capacitance are added into the latter, both of the real and imaginary parts of its effective parameter become tunable.

APPENDIX B: DETAILS IN THE DERIVATION OF TRANSFER MATRIX METHOD

In the Sec. II, we employ the transfer matrix method to derive the band structure and transmission. Here, we add details about its derivation.

In our transfer matrix analytical approach [43,44], we describe the flexural wave propagation by using the Timoshenko beam theory based on the following equation [45]:

$$\frac{EI}{\rho S}\frac{\partial^4 w(x,t)}{\partial x^4} - \frac{I}{S}\left(1+\frac{E}{\mu G}\right)\frac{\partial^4 w(x,t)}{\partial x^2 \partial t^2} + \frac{\partial^2 w(x,t)}{\partial t^2} + \frac{\rho I}{\mu G S}\frac{\partial^4 w(x,t)}{\partial t^4} = 0, \tag{B1}$$

where $w(x,\ t)$ is the vertical displacement; E, G, and ρ are, respectively, Young's modulus, shear modulus, and mass density; $I = bh^3/12$ is the flexural rigidity; $S = bh$ is the cross-sectional area; and $\mu = \frac{5}{6}$ is a shear correction factor for rectangular section.

The time-harmonic solution of Eq. (B1) in the nth layer is composed of two propagating and two evanescent waves (with real and imaginary wave numbers, respectively) in two axial directions. It can be written as

$$w_n(x) = A_n e^{q_1 x} + B_n e^{q_2 x} + C_n e^{q_3 x} + D_n e^{q_4 x}, \tag{B2}$$

where $q_j = (-1)^{j-1}\sqrt{\frac{\alpha+(-1)^{j(j+1)/2}\sqrt{\alpha^2+4\beta}}{2}}$, $j = 1,\ \ldots,\ 4$ denote the four wave numbers, $\alpha = -\omega^2\rho(\frac{1}{E}+\frac{1}{\mu G})$, $\beta = \omega^2\rho(\frac{S}{EI} - \frac{\omega^2\rho}{\mu E G})$, ω is the angular frequency, and A_n, B_n, C_n, and D_n are arbitrary coefficients that should be determined from the boundary conditions. Further, the displacement, rotation angle, bending moment, and shear force of the nth layer can be expressed as

$$\begin{bmatrix} w_n(x) \\ \varphi_n(x) \\ M_n(x) \\ V_n(x) \end{bmatrix} = \begin{bmatrix} e^{q_1 x} & e^{q_2 x} & e^{q_3 x} & e^{q_4 x} \\ q_1 e^{q_1 x} & q_2 e^{q_2 x} & q_3 e^{q_3 x} & q_4 e^{q_4 x} \\ EIq_1^2 e^{q_1 x} & EIq_2^2 e^{q_2 x} & EIq_3^2 e^{q_3 x} & EIq_4^2 e^{q_4 x} \\ EIq_1^3 e^{q_1 x} & EIq_2^3 e^{q_2 x} & EIq_3^3 e^{q_3 x} & EIq_4^3 e^{q_4 x} \end{bmatrix} \mathbf{U}_n, \tag{B3}$$

where $\mathbf{U}_n$ is the column vector formed by A_n, B_n, C_n, and D_n. For the interface between layers n and $n+1$, we apply the continuity conditions on w_n, φ_n, M_n, and V_n as follows:

$$\begin{bmatrix} w_n(x_i) \\ \varphi_n(x_i) \\ M_n(x_i) \\ V_n(x_i) \end{bmatrix} = \begin{bmatrix} w_{n+1}(x_i) \\ \varphi_{n+1}(x_i) \\ M_{n+1}(x_i) \\ V_{n+1}(x_i) \end{bmatrix}, \tag{B4}$$

where x_i is the x coordinate at the interface. Then we have $\mathbf{P}_n\mathbf{U}_n = \mathbf{Q}_{n+1}\mathbf{U}_{n+1}$, $(n = 1,\ \ldots,\ 4)$, where $\mathbf{P}_n$ denotes the right boundary matrix of the layer n and $\mathbf{Q}_{n+1}$ denotes the left boundary matrix of the layer $n+1$. They can be expressed as

$$\mathbf{P}_n = \begin{bmatrix} e^{q_1^n x_i} & e^{q_2^n x_i} & e^{q_3^n x_i} & e^{q_4^n x_i} \\ q_1^n e^{q_1^n x_i} & q_2^n e^{q_2^n x_i} & q_3^n e^{q_3^n x_i} & q_4^n e^{q_4^n x_i} \\ E_n I_n (q_1^n)^2 e^{q_1^n x_i} & E_n I_n (q_2^n)^2 e^{q_2^n x_i} & E_n I_n (q_3^n)^2 e^{q_3^n x_i} & E_n I_n (q_4^n)^2 e^{q_4^n x_i} \\ E_n I_n (q_1^n)^3 e^{q_1^n x_i} & E_n I_n (q_2^n)^3 e^{q_2^n x_i} & E_n I_n (q_3^n)^3 e^{q_3^n x_i} & E_n I_n (q_4^n)^3 e^{q_4^n x_i} \end{bmatrix},$$

$$\mathbf{Q}_{n+1} = \begin{bmatrix} e^{q_1^{n+1} x_i} & e^{q_2^{n+1} x_i} & e^{q_3^{n+1} x_i} & e^{q_4^{n+1} x_i} \\ q_1^{n+1} e^{q_1^{n+1} x_i} & q_2^{n+1} e^{q_2^{n+1} x_i} & q_3^{n+1} e^{q_3^{n+1} x_i} & q_4^{n+1} e^{q_4^{n+1} x_i} \\ E_{n+1} I_{n+1} (q_1^{n+1})^2 e^{q_1^{n+1} x_i} & E_{n+1} I_{n+1} (q_2^{n+1})^2 e^{q_2^{n+1} x_i} & E_{n+1} I_{n+1} (q_3^{n+1})^2 e^{q_3^{n+1} x_i} & E_{n+1} I_{n+1} (q_4^{n+1})^2 e^{q_4^{n+1} x_i} \\ E_{n+1} I_{n+1} (q_1^{n+1})^3 e^{q_1^{n+1} x_i} & E_{n+1} I_{n+1} (q_2^{n+1})^3 e^{q_2^{n+1} x_i} & E_{n+1} I_{n+1} (q_3^{n+1})^3 e^{q_3^{n+1} x_i} & E_{n+1} I_{n+1} (q_4^{n+1})^3 e^{q_4^{n+1} x_i} \end{bmatrix}, \tag{B5}$$

where the specific values of E, I, and q are determined by the material of the layer.

By employing the transfer between different layers, we obtain

$$\mathbf{T}\mathbf{U}_1 = \mathbf{U}_5, \tag{B6}$$

where $\mathrm{T} = \mathbf{Q}_5^{-1}\mathbf{P}_4\mathbf{Q}_4^{-1}\mathbf{P}_3\mathbf{Q}_3^{-1}\mathbf{P}_2\mathbf{Q}_2^{-1}\mathbf{P}_1$ is the transfer matrix. Applying the Bloch periodicity condition yields

$$\mathbf{Q}_1\mathbf{U}_1 = e^{ika}\mathbf{P}_5\mathbf{U}_5, \tag{B7}$$

where k is the Bloch wave number. By combining Eqs. (B6) and (B7), we obtain the eigenequation as

follows:

$$\left|\mathbf{Q}_1 - e^{ika}\mathbf{P}_5\mathbf{T}\right| = 0. \tag{B8}$$

By solving Eq. (B8), we can obtain the band structure marked in red solid lines in Fig. 1(c).

Similar to the eigenfrequency calculation, we employ the transfer matrix method to calculate the transmission spectra of finite structures. According to Eq. (B6), we obtain the relationship between the left- and right-hand side coefficients of the finite phononic beam as $\mathbf{T}^N\mathbf{U}_1 = \mathbf{U}_{4N+1}$, where $\mathbf{T}^N = \prod_{i=1}^{4N}\mathbf{Q}_{4N+2-i}^{-1}\mathbf{P}_{4N+1-i}$, and N is the number of units. By rearranging the system of linear equations, we can rewrite it as follows:

$$\mathbf{S}\begin{bmatrix} B_1 \\ D_1 \\ A_{4N+1} \\ C_{4N+1} \end{bmatrix} = \begin{bmatrix} A_1 \\ C_1 \\ B_{4N+1} \\ D_{4N+1} \end{bmatrix}, \tag{B9}$$

where

$$\mathbf{S} = \begin{bmatrix} -T_{(11)} & -T_{(13)} & 0 & 0 \\ -T_{(21)} & -T_{(23)} & 1 & 0 \\ -T_{(31)} & -T_{(33)} & 0 & 0 \\ -T_{(41)} & -T_{(43)} & 0 & 1 \end{bmatrix}^{-1} \begin{bmatrix} T_{(12)} & T_{(14)} & -1 & 0 \\ T_{(22)} & T_{(24)} & 0 & 0 \\ T_{(32)} & T_{(34)} & 0 & -1 \\ T_{(42)} & T_{(44)} & 0 & 0 \end{bmatrix} \tag{B10}$$

is the scattering matrix, B_1, D_1, A_{4N+1}, and C_{4N+1} are the incident coefficients; A_1, C_1, B_{4N+1}, and D_{4N+1} are the outcoming coefficients; and $T_{(ij)}$ denote the elements in the transfer matrix $\mathbf{T}^N$. Considering a left incidence propagating wave, i.e., $B_1 = 1$, we can obtain the reflection coefficients for the propagating wave $r_p = |S_{(11)}|$ and evanescent wave $r_e = |S_{(21)}|$ and the transmission coefficients of propagating wave $t_p = |S_{(31)}|$ and evanescent wave $t_e = |S_{(41)}|$, wherein t_p is used for the transmission spectra calculation of Fig. 2, while $\arg[S_{(11)}]$ is used for the reflection phases calculation of Fig. 3.

APPENDIX C: DWP, WDL, AND WHR FORMED BY DIFFERENT BANDS

First, we explain the type of degenerate points formed by band crossing through the derivation of the system Hamiltonian. As we stated in Sec. II, the bands are quadratic along k and ξ but linear along ζ near the degenerate point $(0, 0, \pi/a)$. We now consider the Taylor expansion of Eq. (2) at point $(0,\ 0,\ \pi/a)$ in three momentum directions. Equation (2) is written as

$$\tilde{\omega}_{1,2}(\xi, \zeta, k) = \omega_0 - \Gamma_0 i \pm \sqrt{4\kappa_0^2\left[\left(\cos\frac{ka}{2}\right)^2 + n^2\xi^2\left(\sin\frac{ka}{2}\right)^2\right] - (\tau\gamma - m\omega_0\zeta i)^2}. \tag{C1}$$

The Taylor expansion is expressed as

$$\tilde{\omega}_\delta(\delta) = \tilde{\omega}_\delta(\delta_0) + \tilde{\omega}'_\delta(\delta_0)(\delta - \delta_0) + \frac{\tilde{\omega}''_\delta(\delta_0)}{2}(\delta - \delta_0)^2 + o[(\delta - \delta_0)^2], \tag{C2}$$

where δ denotes k, ξ, or ζ; and δ_0 is respectively π/a and 0. Calculating the partial derivative of k, ξ, and ζ for $\tilde{\omega}_\delta$, respectively, we obtain

$$\tilde{\omega}'_k\left(0, 0, \frac{\pi}{a}\right) = 0, \tag{C3a}$$

$$\tilde{\omega}''_k\left(0, 0, \frac{\pi}{a}\right) = \pm\frac{a^2\kappa_0^2}{\tau\gamma i}, \tag{C3b}$$

$$\tilde{\omega}'_\xi\left(0, 0, \frac{\pi}{a}\right) = 0, \tag{C3c}$$

$$\tilde{\omega}''_\xi\left(0, 0, \frac{\pi}{a}\right) = \pm\frac{4\kappa_0^2 n^2}{\tau\gamma i}, \tag{C3d}$$

$$\tilde{\omega}'_\zeta\left(0, 0, \frac{\pi}{a}\right) = \pm m\omega_0. \tag{C3e}$$

Therefore, the quadratic term dominates along the k and ξ directions, while the linear term dominates along the ζ direction. Since there are quadratic dispersions in at least one momentum plane, this indicates that this degenerate point belongs to the DWP [12].

Next, we focus on slicing the band structures, as shown in Fig. 5(a). The bands cut by the gray plane corresponding to different ζ form the orange dashed lines in Fig. 2 and assist us in observing the DWP and WDL in the transmission spectra. Figure 5(b) shows the WDLs and WHRs corresponding to different γ's in the plane $\zeta = 0$. The frequencies of WDLs are slightly bent upward at both ends of positive and negative ξ. In the reflection phase calculation, we choose the middle frequency of the WDL as the incident wave frequency.

Finally, we show more details about DWPs which are marked by the color balls in Fig. 1(b). The band structures corresponding to the three pairs of synthetic parameters are summarized in Fig. 6(a). The configuration corresponding to the red balls causes the degeneracy of the first and second bands as well as the third and fourth bands at the edge of the BZ. Among them, the DWPs formed by the first and second bands have already been discussed in the main text, while the DWP formed by the third and fourth bands is shown in Fig. 6(c). The configuration corresponding to the green ball causes the degeneracy of the second and third bands at the center of the BZ, while the configuration corresponding to the yellow ball causes the degeneracy of the third and fourth bands at the edge of the BZ. These DWPs are shown in Figs. 6(b) and 6(c).

When the nonhermiticity factor is introduced into the system, all DWPs shown in Fig. 6 evolve into WDLs for the real parts of the frequencies [see Figs. 7(a) and 7(c)] and WHRs for their imaginary parts [see Figs. 7(b) and 7(d)]. As the

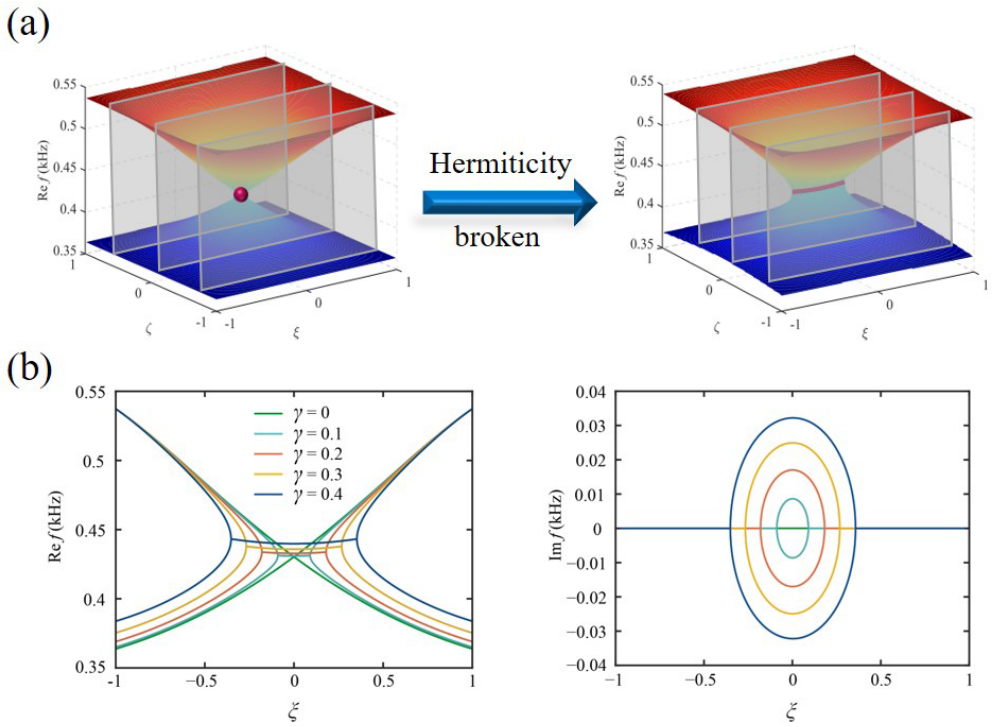

FIG. 5. (a) Schematic diagram of different ζ cutting band structures. (b) Observe the Weyl degenerate line (WDL; left panel) and the Weyl hollow ring (WHR; right panel) corresponding to different non-Hermite factors γ in the $\zeta = 0$ plane.

green DWPs are close to the synthetic parameter boundary, the parts of the WDLs and WHRs outside the parameter boundary are missing. The middle frequencies of green and yellow WDLs are, respectively, 1804 and 4094 Hz. Compared with the DWP frequencies, the introduction of nonhermiticity leads to a slight increase of frequency.

APPENDIX D: REFLECTION PHASE VORTICES AND FERMI ARCS AROUND DIFFERENT DWPS

Figure 8(a) shows the reflection phase in (ξ, ζ) space at the frequency 1804 Hz of DWPs formed by second and third bands in a hermitic situation. Since both DWPs have a topological charge of 2 in the synthetic parameter space, the synthetic Fermi arcs still terminate at the parameter boundary, as shown by the green and magenta dashed lines. In a non-Hermitian case, the vortex associated with the reflection phase is shifted to $\xi < 0$ and $\xi > 0$ depending on the positive or negative imaginary part of the excitation frequency [see Figs. 8(b) and 8(c)]. Also, the reflection phases exhibit opposite signs in these two cases. Notice that, in Figs. 8(b) and 8(c), the vortex centers are close to the space parameter boundary, and the winding of the reflection phase cannot be fully observed.

Figure 8(d) shows the reflection phase in (ξ, ζ) space at the frequency of 3995 Hz of DWPs formed by the third and fourth bands, while Figs. 8(e)–8(f) show the reflection phase in a nonhermitic system. In addition to some phenomena that

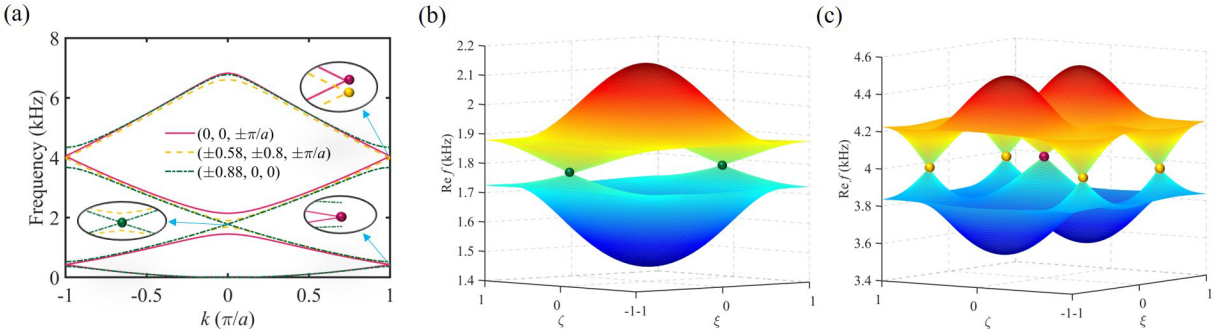

FIG. 6. (a) Three band structures with degenerate points in synthetic parameter space. (b) The double Weyl point (DWP) formed at $(\pm 0.88, 0, 0)$ by the second and third bands; the frequency is 1785 Hz. (c) The DWP formed at $(0, 0, \pm\pi/a)$ and $(\pm 0.58, \pm 0.8, \pm\pi/a)$ by the second and third bands; the frequency is 3995 Hz. The colors of the surfaces in (b) and (c) indicate the frequency, with an increase from blue to red.

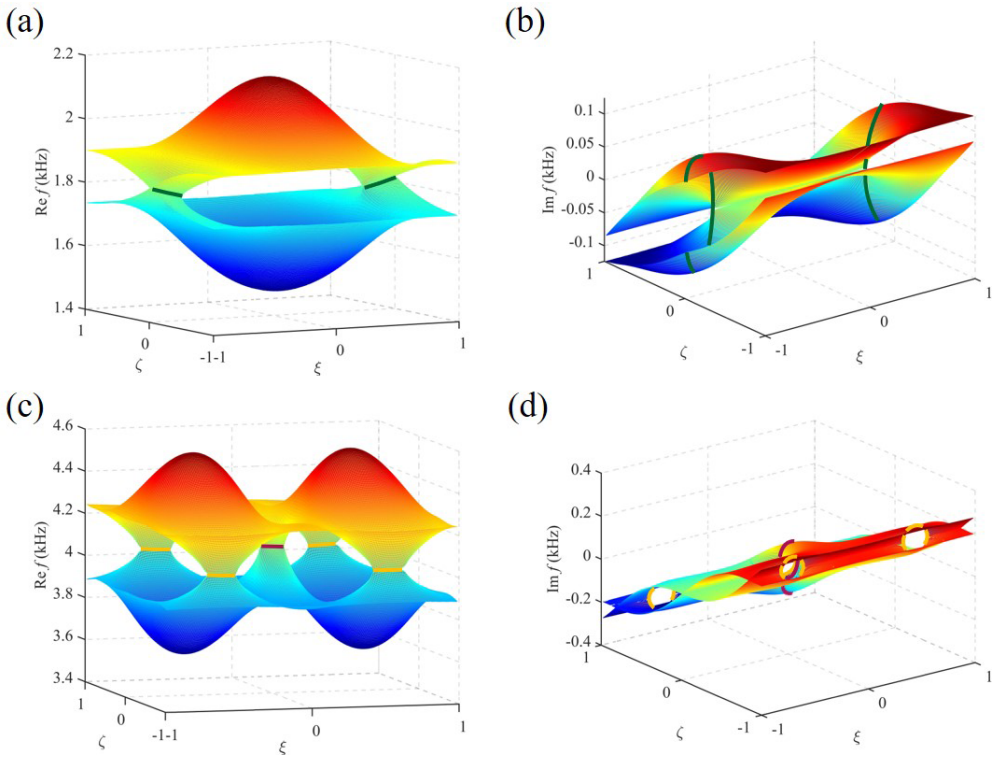

FIG. 7. Double Weyl point (DWP) evolution caused by the introduction of nonhermiticity. (a) and (b) Weyl degenerate line (WDL) and Weyl hollow ring (WHR) formed by the second and third bands. (c) and (d) WDL and WHR formed by the third and fourth bands. The colors of the surfaces indicate the frequency, with an increase from blue to red.

have been discussed, this reflection phase diagram has both clockwise and counterclockwise reflection phase vortices. The opposite topological charges possessed by the vortices lead to the appearance of complete synthetic Fermi arcs [see the green and magenta dashed lines connecting red and yellow balls in Figs. 8(d)–8(f)].

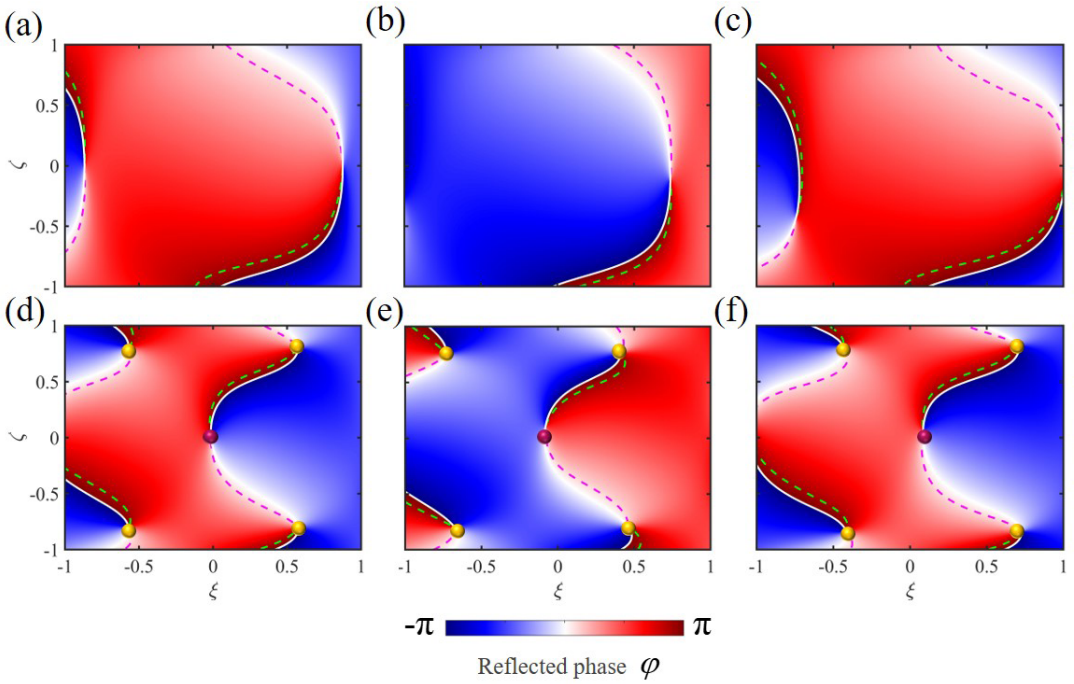

FIG. 8. Reflection phase vortex structures in synthetic $\xi-\zeta$ space, excited at the double Weyl point (DWP) frequency (a) 1785 Hz and (d) 3995 Hz and the Weyl degenerate line (WDL) frequency (b) and (c) $(1804 \pm 89i)$ and (e) and (f) $(4094 \pm 116i)$ Hz.

[1] X. Wan, A. M. Turner, A. Vishwanath, and S. Y. Savrasov, Topological semimetal and Fermi-arc surface states in the electronic structure of pyrochlore iridates, Phys. Rev. B **83**, 205101 (2011).

[2] S. Y. Xu, I. Belopolski, N. Alidoust, M. Neupane, G. Bian, C. Zhang, R. Sankar, G. Chang, Z. Yuan, C. C. Lee *et al.*, Discovery of a Weyl fermion semimetal and topological Fermi arcs, Science **349**, 613 (2015).

[3] A. A. Soluyanov, D. Gresch, Z. Wang, Q. Wu, M. Troyer, X. Dai, and B. A. Bernevig, Type-II Weyl semimetals, Nature (London) **527**, 495 (2015).

[4] B. Q. Lv, N. Xu, H. M. Weng, J. Z. Ma, P. Richard, X. C. Huang, L. X. Zhao, G. F. Chen, C. E. Matt, F. Bisti *et al.*, Observation of Weyl nodes in TaAs, Nat. Phys. **11**, 724 (2015).

[5] M. Z. Hasan and C. L. Kane, Colloquium: Topological insulators, Rev. Mod. Phys. **82**, 3045 (2010).

[6] B. Q. Lv, H. M. Weng, B. B. Fu, X. P. Wang, H. Miao, J. Ma, P. Richard, X. C. Huang, L. X. Zhao, G. F. Chen *et al.*, Experimental Discovery of Weyl Semimetal TaAs, Phys. Rev. X **5**, 031013 (2015).

[7] L. Lu, Z. Wang, D. Ye, L. Ran, L. Fu, J. D. Joannopoulos, and M. Soljacic, Experimental observation of Weyl points, Science **349**, 622 (2015).

[8] F. Li, X. Huang, J. Lu, J. Ma, and Z. Liu, Weyl points and Fermi arcs in a chiral phononic crystal, Nat. Phys. **14**, 30 (2017).

[9] M. Xiao, W.-J. Chen, W.-Y. He, and C. T. Chan, Synthetic gauge flux and Weyl points in acoustic systems, Nat. Phys. **11**, 920 (2015).

[10] H. He, C. Qiu, L. Ye, X. Cai, X. Fan, M. Ke, F. Zhang, and Z. Liu, Topological negative refraction of surface acoustic waves in a Weyl phononic crystal, Nature (London) **560**, 61 (2018).

[11] X. Lyu, H. Li, M. He, Q. Ding, and T. Yang, Observation of the Weyl points and topological edge states in a synthetic Weyl elastic crystal, Appl. Phys. Lett. **121**, 122202 (2022).

[12] Y.-T. Wang and Y.-W. Tsai, Multiple Weyl and double-Weyl points in an elastic chiral lattice, New J. Phys. **20**, 083031 (2018).

[13] M.-L. Chang, M. Xiao, W.-J. Chen, and C. T. Chan, Multiple Weyl points and the sign change of their topological charges in woodpile photonic crystals, Phys. Rev. B **95**, 125136 (2017).

[14] S. M. Huang, S. Y. Xu, I. Belopolski, C. C. Lee, G. Chang, T. R. Chang, B. Wang, N. Alidoust, G. Bian, M. Neupane *et al.*, New type of Weyl semimetal with quadratic double Weyl fermions, Proc. Natl. Acad. Sci. USA **113**, 1180 (2016).

[15] Q. Wang, M. Xiao, H. Liu, S. Zhu, and C. T. Chan, Optical Interface States Protected by Synthetic Weyl Points, Phys. Rev. X **7**, 031032 (2017).

[16] X. Fan, C. Qiu, Y. Shen, H. He, M. Xiao, M. Ke, and Z. Liu, Probing Weyl Physics with One-Dimensional Sonic Crystals, Phys. Rev. Lett. **122**, 136802 (2019).

[17] H. Gao, H. Xue, Q. Wang, Z. Gu, T. Liu, J. Zhu, and B. Zhang, Observation of topological edge states induced solely by non-Hermiticity in an acoustic crystal, Phys. Rev. B **101**, 180303(R) (2020).

[18] H. Wang, X. Zhang, J. Hua, D. Lei, M. Lu, and Y. Chen, Topological physics of non-Hermitian optics and photonics: A review, J. Opt. **23**, 123001 (2021).

[19] Z. Gu, H. Gao, T. Liu, S. Liang, S. An, Y. Li, and J. Zhu, Topologically Protected Exceptional Point with Local Non-Hermitian Modulation in an Acoustic Crystal, Phys. Rev. Appl. **15**, 014025 (2021).

[20] R. Cai, Y. Jin, Y. Li, T. Rabczuk, Y. Pennec, B. Djafari-Rouhani, and X. Zhuang, Exceptional Points and Skin Modes in Non-Hermitian Metabeams, Phys. Rev. Appl. **18**, 014067 (2022).

[21] Y. Jin, W. Zhong, R. Cai, X. Zhuang, Y. Pennec, and B. Djafari-Rouhani, Non-Hermitian skin effect in a phononic beam based on piezoelectric feedback control, Appl. Phys. Lett. **121**, 022202 (2022).

[22] M. Farhat, P. Y. Chen, S. Guenneau, and Y. Wu, Self-dual singularity through lasing and antilasing in thin elastic plates, Phys. Rev. B **103**, 134101 (2021).

[23] G. Trainiti, Y. Xia, J. Marconi, G. Cazzulani, A. Erturk, and M. Ruzzene, Time-Periodic Stiffness Modulation in Elastic Metamaterials for Selective Wave Filtering: Theory and Experiment, Phys. Rev. Lett. **122**, 124301 (2019).

[24] K. Yi, M. Ouisse, E. Sadoulet-Reboul, and G. Matten, Active metamaterials with broadband controllable stiffness for tunable band gaps and non-reciprocal wave propagation, Smart Mater. Struct. **28**, 065025 (2019).

[25] W. Zhou, B. Wu, Z. Chen, W. Chen, C. W. Lim, and J. N. Reddy, Actively controllable topological phase transition in homogeneous piezoelectric rod system, J. Mech. Phys. Solids **137**, 103824 (2020).

[26] Q. Wu, Y. Chen, and G. Huang, Asymmetric scattering of flexural waves in a parity-time symmetric metamaterial beam, J. Acoust. Soc. Am. **146**, 850 (2019).

[27] Y. Chen, G. Hu, and G. Huang, A hybrid elastic metamaterial with negative mass density and tunable bending stiffness, J. Mech. Phys. Solids **105**, 179 (2017).

[28] Z. Hou and B. Assouar, Tunable elastic parity-time symmetric structure based on the shunted piezoelectric materials, J. Appl. Phys. **123**, 085101 (2018).

[29] A. Darabi, M. Collet, and M. J. Leamy, Experimental realization of a reconfigurable electroacoustic topological insulator, Proc. Natl. Acad. Sci. USA **117**, 16138 (2020).

[30] C. Sugino, M. Ruzzene, and A. Erturk, Digitally Programmable Resonant Elastic Metamaterials, Phys. Rev. Appl. **13**, 061001 (2020).

[31] J. Marconi, E. Riva, M. Di Ronco, G. Cazzulani, F. Braghin, and M. Ruzzene, Experimental Observation of Nonreciprocal Band Gaps in a Space-Time-Modulated Beam Using a Shunted Piezoelectric Array, Phys. Rev. Appl. **13**, 031001 (2020).

[32] C. M. Bender, B. K. Berntson, D. Parker, and E. Samuel, Observation of PT phase transition in a simple mechanical system, Am. J. Phys. **81**, 173 (2013).

[33] M. A. Miri and A. Alu, Exceptional points in optics and photonics, Science **363**, eaar7709 (2019).

[34] J. Doppler, A. A. Mailybaev, J. Bohm, U. Kuhl, A. Girschik, F. Libisch, T. J. Milburn, P. Rabl, N. Moiseyev, and S. Rotter, Dynamically encircling an exceptional point for asymmetric mode switching, Nature (London) **537**, 76 (2016).

[35] Z. Lin, H. Ramezani, T. Eichelkraut, T. Kottos, H. Cao, and D. N. Christodoulides, Unidirectional Invisibility Induced by PT-symmetric Periodic Structures, Phys. Rev. Lett. **106**, 213901 (2011).

[36] A. Cerjan, S. Huang, M. Wang, K. P. Chen, Y. Chong, and M. C. Rechtsman, Experimental realization of a Weyl exceptional ring, Nat. Photonics **13**, 623 (2019).

[37] J. Liu, Z. Li, Z. Chen, W. Tang, A. Chen, B. Liang, G. Ma, and J. Cheng, Experimental Realization of Weyl Exceptional Rings in a Synthetic Three-Dimensional Non-Hermitian Phononic Crystal, Phys. Rev. Lett. **129**, 084301 (2022).

[38] Y. Jin, Y. Pennec, B. Bonello, H. Honarvar, L. Dobrzynski, B. Djafari-Rouhani, and M. I. Hussein, Physics of surface vibrational resonances: Pillared phononic crystals, metamaterials, and metasurfaces, Rep. Prog. Phys. **84**, 086502 (2021).

[39] Y. Jin, L. He, Z. Wen, B. Mortazavi, H. Guo, D. Torrent, B. Djafari-Rouhani, T. Rabczuk, X. Zhuang, and Y. Li, Intelligent on-demand design of phononic metamaterials, Nanophotonics **11**, 439 (2022).

[40] H. Fan, H. Gao, S. An, Z. Gu, S. Liang, Y. Zheng, and T. Liu, Hermitian and non-hermitian topological edge states in one-dimensional perturbative elastic metamaterials, Mech. Syst. Signal Process. **169**, 108774 (2022).

[41] A. Cerjan, M. Xiao, L. Yuan, and S. Fan, Effects of non-Hermitian perturbations on Weyl Hamiltonians with arbitrary topological charges, Phys. Rev. B **97**, 075128 (2018).

[42] M. Xiao, Z. Q. Zhang, and C. T. Chan, Surface Impedance and Bulk Band Geometric Phases in One-Dimensional Systems, Phys. Rev. X **4**, 021017 (2014).

[43] L. He, H. Guo, Y. Jin, X. Zhuang, T. Rabczuk, and Y. Li, Machine-learning-driven on-demand design of phononic beams, Sci. China Phys. Mech. Astron. **65**, 214612 (2022).

[44] Muhammad, W. Zhou, and C. W. Lim, Topological edge modeling and localization of protected interface modes in 1D phononic crystals for longitudinal and bending elastic waves, Int. J. Mech. Sci. **159**, 359 (2019).

[45] A. Diaz-de-Anda, A. Pimentel, J. Flores, A. Morales, L. Gutierrez, and R. A. Mendez-Sanchez, Locally periodic Timoshenko rod: Experiment and theory, J. Acoust. Soc. Am. **117**, 2814 (2005).